Metal-induced fluorescence properties of three-dimensionally ordered macroporous silver inverse opal platforms

Weon-Sik Chae, Myung-Jin Lee, Kisun Kim, Jerome K. Hyun, and Seokwoo Jeon

Citation: Applied Physics Letters **108**, 071909 (2016); doi: 10.1063/1.4942397
View online: http://dx.doi.org/10.1063/1.4942397
View Table of Contents: http://scitation.aip.org/content/aip/journal/apl/108/7?ver=pdfcov
Published by the AIP Publishing

Metal-induced fluorescence properties of three-dimensionally ordered macroporous silver inverse opal platforms

Weon-Sik Chae,[1,a)] Myung-Jin Lee,[2] Kisun Kim,[3] Jerome K. Hyun,[4] and Seokwoo Jeon[3,a)]
[1]*Analysis Research Division, Daegu Center, Korea Basic Science Institute, Daegu 702-701, South Korea*
[2]*Gangneung Center, Korea Basic Science Institute, Gangneung 210-702, South Korea*
[3]*Department of Materials Science and Engineering, KAIST Institute for the Nanocentury, Korea Advanced Institute of Science and Technology (KAIST), Daejeon 305-338, South Korea*
[4]*Department of Chemistry and Nano Science, Ewha Womans University, Seoul 120-750, South Korea*

(Received 15 December 2015; accepted 7 February 2016; published online 19 February 2016)

This study examined the metal-induced fluorescence properties of three-dimensionally ordered macroporous silver inverse opal (IO) films. Electrochemically synthesized silver IO films with a micrometer cavity exhibited notable fluorescence enhancement at the silver frame, and a decrease in fluorescence lifetime. Numerical calculations supported the observations of a higher fluorescence efficiency at the frame than in the cavity. © *2016 AIP Publishing LLC*.
[http://dx.doi.org/10.1063/1.4942397]

Fluorescent molecules near a plasmonic metal surface possess interesting emission properties, which are manifested by modulations in intensity, wavelength, and lifetime.[1] In particular, nanostructured plasmonic metals enable remarkable amplification of the optical characteristics due to enhanced electromagnetic interactions between the adjacent fluorophores and metal surface.[2–7] One of the most frequently observed phenomena is the so-called optical antenna effect, in which the accumulation of an electric field around a metal surface reinforces the excitation probability for molecules, typically resulting in amplified emission.[8–12] Furthermore, plasmonic metals provide an additional direct radiative pathway for excited electrons, resulting in enhanced quantum yields and blue-shifted emission.[1,13,14]

On the other hand, the strong coupling of fluorophores with a metal at the interface can also result in emission quenching.[15–17] The photoexcited electrons in a molecule can be transferred easily to bound metal nanoparticles, disrupting the radiative recombination. According to theoretical calculations[18,19] and experimental observations,[20,21] larger particles and skeletons are suitable for reducing the absorption cross-section of a metal while increasing the scattering cross-section. This minimizes emission quenching and enhances the fluorescence (FL) due to the optical antenna effect.[22,23]

A film-type porous skeleton composed of a plasmonic metal has obvious advantages. Porous metal films have a non-dispersible robust configuration in a fluidic system compared to mobile nanoparticles in solution, thereby reducing the accompanying secondary problems, such as environmental and cytotoxic issues for further applications. The current technology provides versatile fabrication routes via chemical reduction,[24,25] electrochemical deposition,[26–28] and evaporation[29,30] for forming and removing templates to prepare porous metal skeletons. Recently, three-dimensionally ordered macroporous (3DOM) materials with a range of compositions were prepared successfully via a colloidal opal templating route.[24,26,28,31] The noble metal 3DOM structures have been proven to be highly efficient as substrates for surface-enhanced Raman scattering.[3,6,27] Nevertheless, 3DOM materials have not been applied to the study of metal-induced FL (MIF).

This study examined the MIF characteristics of the 3DOM Ag inverse opal (IO) skeletons, which were prepared by electrochemical deposition using colloidal opals as the template film (see supplementary material[32]). A standard fluorescent dye molecule, rhodamine 123, in solution was introduced to the porous Ag IO skeletons. The FL properties were examined using time-resolved FL lifetime imaging microscopy (FLIM), where the position-dependent MIF modulations in intensity and lifetime could be measured directly. These results showed that the 3DOM Ag IO frame performs as a stable and uniform platform for FL enhancement.

Figure 1 shows a scanning electron microscopy (SEM) image of the fabricated Ag IO film. The image was obtained after the complete removal of well-ordered polystyrene (PS) templates. The Ag IO shows a hexagonal array of cavities with excellent regularity. The IO skeleton grown on a Si wafer was also examined by X-ray diffraction (XRD). The measured XRD pattern showed peaks at 38.18° and 81.70° in 2θ, which is in good agreement with the face-centered-cubic (fcc) Ag phase (JCPDS No. 04-0783). The plasmonic absorption peak was observed to extend beyond 500 nm (inset of Fig. 1(b)), which is well coherent with the absorption ($\lambda_{abs} = 507$ nm) and fluorescence ($\lambda_{em} = 529$ nm) of rhodamine 123.

The FLIM technique has attracted considerable attention in a wide range of fields, because it provides precise spatial information of the FL lifetime in 2D or 3D space.[33] The spatial inhomogeneity of the FL lifetime in nanomaterials and cells can be resolved clearly by FLIM.[34,35] Figure 2(a) shows FLIM images of rhodamine 123 on the top surface of the Ag IO, showing a shorter lifetime than that of bulk rhodamine 123, whose FLIM image is shown in the inset of Figure 2(a). The FL lifetime of bulk rhodamine 123 in aqueous solution (0.01 mM) was estimated to be 4.01 ± 0.03 ns with a single

[a)]Authors to whom correspondence should be addressed. Electronic addresses: wschae@kbsi.re.kr and jeon39@kaist.ac.kr.

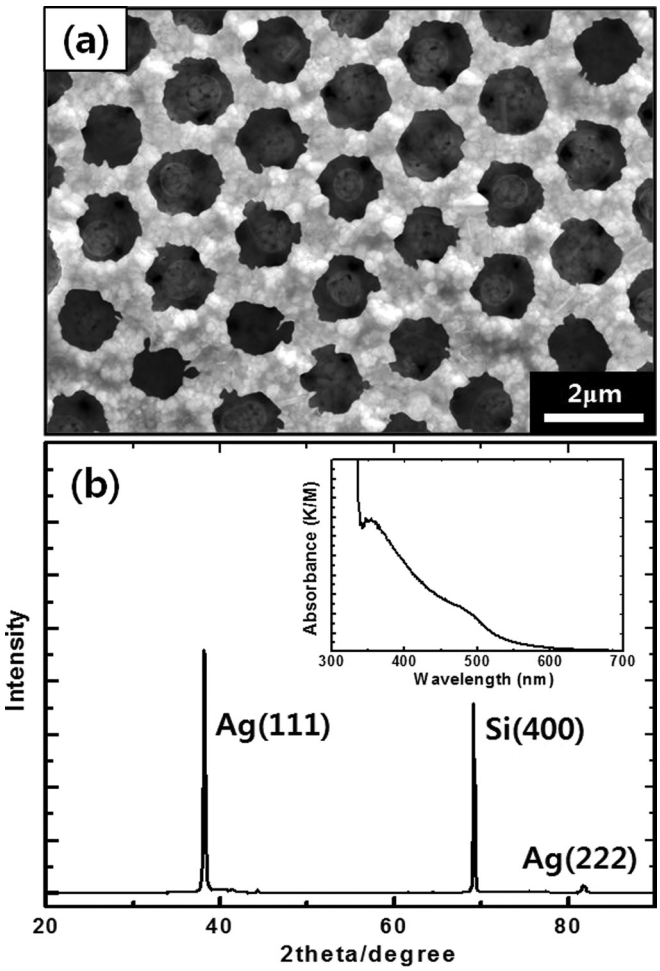

FIG. 1. (a) SEM image of the Ag IO. (b) X-ray diffraction pattern of the Ag IO grown on a Si wafer. The peak at 69.09° in 2θ was assigned to the Si(400) plane. The inset in (b) is the absorption spectrum of the Ag IO film.

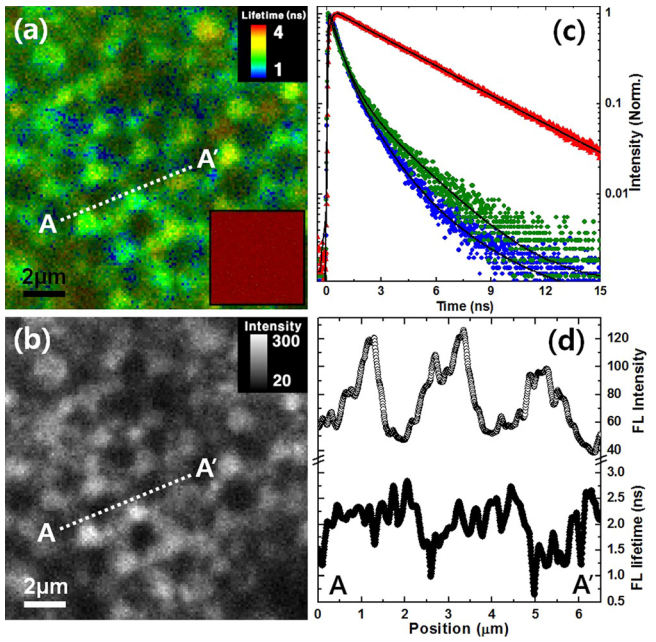

FIG. 2. (a) Averaged FLIM image of rhodamine 123 near Ag IO, the inset in (a) is the FLIM image of rhodamine 123 aqueous solution with a FL lifetime of 4.01 ns, (b) photon counting FL image, (c) time-resolved FL decays of rhodamine 123 near the frame (blue dots) and inside the cavity (green dots) of the Ag IO as well as the bulk rhodamine 123 aqueous solution (red triangles), (d) line profiles of FL in intensity (open circles) and lifetime (closed circles) at the dotted lines, as indicated in (a) and (b).

exponential component (Fig. 2(c)). The dye molecule near the Ag IO surface frame has a relatively shorter lifetime than that in the cavity region. For the rhodamine 123 molecules near the Ag IO frame, the intensity-weighted average lifetime, $\langle\tau\rangle = \sum_i A_i\tau_i^2 / \sum_i A_i\tau_i$, where A is the amplitude and τ is the lifetime, was reduced dramatically to 1.67 ± 0.10 ns, which can be divided into two exponential sub-components of 0.39 ± 0.02 (92% in amplitude; τ_1) and 3.37 ± 0.07 ns (8% in amplitude; τ_2). Compared to the bulk FL lifetime, the short-lived component (τ_1) was reduced by 90%, whereas the long-lived component (τ_2) was reduced by 16%. It is noteworthy that this dramatically reduced lifetime is much shorter than the average lifetime of 3.11 ± 0.25 ns observed for a dye on a planar Ag film (see Fig. S1 of supplementary material[32]). In the planar Ag film, the slightly reduced lifetime of the dye was attributed to local fluorescence modulation by the surface roughness formed during electrochemical deposition.

On the other hand, rhodamine 123 located inside the micrometer-sized cavities showed relatively longer lifetimes than that near the frame; $\langle\tau\rangle$ was 2.30 ± 0.10 ns with two sub-components of 0.40 ± 0.03 (80% in amplitude; τ_1) and 3.24 ± 0.10 ns (20% in amplitude; τ_2). Whenever rhodamine 123 was located near the cavity or frame, each sub-component lifetime was found to be similar within the experimental error. However, the main difference in the average lifetimes between the cavity and the frame comes from the fractional change in amplitude. The FL lifetime of rhodamine 123 near the frame of Ag IO consisted of a higher fraction (92%) of the short-lived component than that of the cavity case (80%). The FL intensity image, which was converted from the corresponding FLIM image based on the photon counts, clearly shows that the top frame of the Ag IO emits more light (Fig. 2(b)). From the cross sectional profile, as indicated by the dotted line in Figures 2(a) and 2(b), the FL lifetime was reduced at the top frame surface, whereas the FL intensity was brighter at the same position, as shown in Figure 2(d).

The FLIM imaging technique with an individual lifetime sub-component clearly demonstrated the spatially resolved FL modulation in intensity for a fixed lifetime component. The averaged FLIM image was calculated separately by the two lifetime components. Figures 3(a) and 3(b) show the recalculated FLIM images for the τ_1 and τ_2 lifetime sub-components, respectively. The short-lived τ_1 was mostly observed at the frame region. However, τ_2 was spread over both frames and cavity regions, even though they were counted slightly more at the frame. An overlay of the short-lived and long-lived images clearly shows the spatial occupation of the two lifetime components over the 3DOM Ag IO. The cavity includes comparable lifetime components of both τ_1 and τ_2; however, the frame region is dominated by τ_1.

In principle, the lifetime (τ_0) and quantum yield (Φ_0) of a fluorophore are given by the following equations:[13,36]

$$\tau_0 = \frac{1}{\Gamma + k_{nr}}, \tag{1}$$

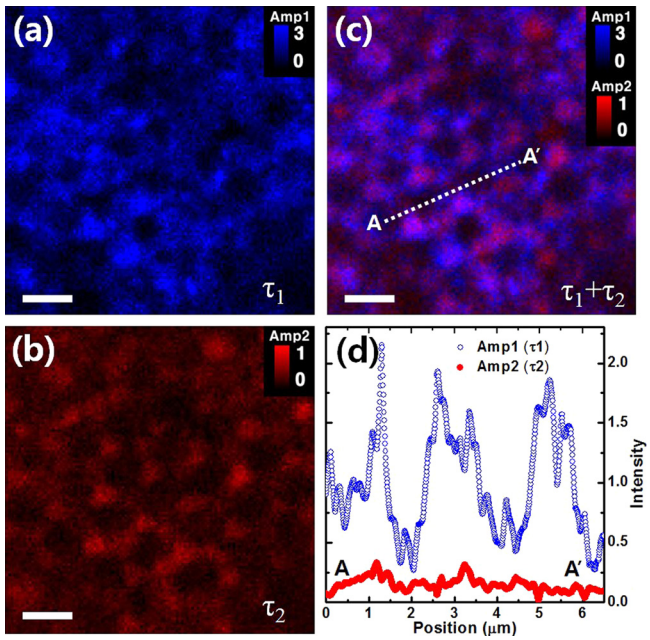

FIG. 3. FL lifetime sub-component images of rhodamine 123 near Ag IO; (a) short-lived (τ_1) component, (b) long-lived (τ_2) component, and (c) overlay of images (a) and (b), and (d) line profiles of the FL intensity of the two sub-components at the dotted line, as indicated in (c). The scale bar is 2 μm.

$$\Phi_0 = \frac{\Gamma}{\Gamma + k_{\mathrm{nr}}}, \tag{2}$$

where Γ and k_{nr} are the radiative and nonradiative decay rates, respectively. When a metal is introduced to a fluorophore system, the lifetime and quantum yield of a fluorophore can be defined by the following equations:[13,37]

$$\tau_{\mathrm{m}} = \frac{1}{\Gamma + \Gamma_m + k_{\mathrm{nr}}}, \tag{3}$$

$$\Phi_{\mathrm{m}} = \frac{\Gamma + \Gamma_{\mathrm{m}}}{\Gamma + \Gamma_{\mathrm{m}} + k_{\mathrm{nr}}}, \tag{4}$$

where Γ_{m} is the metal coupled radiative rate of a fluorophore. Therefore, in the presence of a metal, the FL lifetime is decreased and the quantum yield can be increased. The FL enhancement, which can be accompanied by an increased radiative rate, can occur up to several tens of nanometers away from the metal surface owing to an extension of the electric field.[5] Electron transfer from the dye to the adjacent metal also increases k_{nr}.[15,16] Therefore, it is believed that the observed short-lived lifetime component is attributable to both the metal-enhanced radiative process and dye-to-metal electron transfer, whereas the long-lived component can be attributed to metal-induced radiative rate enhancement around the Ag metal skeleton.

FLIM images were also taken at several hundreds of nanometers below the top surface of the Ag IO (see Fig. S2 of supplementary material[32]). In this case, the cavity region showed high photon counts and simultaneously reduced FL lifetime; $\langle\tau\rangle$ was estimated to be 2.17 ± 0.04 ns. The FL decay consisted of two lifetime components: 0.34 ± 0.03 (88% in amplitude) and 3.48 ± 0.03 ns (12% in amplitude). The averaged lifetime was intermediate between the averaged lifetimes at the frame and the cavity measured at the top surface of the Ag IO.

To better understand the MIF behavior at the frame and the cavity regions of the Ag IO, the electric field distribution of the Ag IO structure was calculated using finite-difference time-domain (FDTD) software (Fig. 4). A Ag cavity array with a 2 μm period was illuminated by a plane wave to model the interaction between the field and Ag IO. The field distribution was observed from a single unit cell at three planes normal to the incident excitation direction. Figures 4(b), 4(c), and 4(d) show the field at 0.2, 0, and -0.5 μm, respectively, from the pivot center of the cavity. At the topmost plane (Fig. 4(b)), the maximum electric field enhancement was achieved at the interface between the cavity and the Ag IO frame, whereas at the bottommost plane (Fig. 4(d)), the maximum electric field enhancement occurred inside the cavity rather than at the frame.

In all cases, the maximum field values are much higher than that from a planar thin Ag film (0.8). These calculations show that the Ag IO structure can locally enhance the electric fields compared to a bare planar Ag film.

To confirm the fluorescence enhancement from the dye molecules, the dipoles resting on the Ag IO structure were considered. The quantum efficiencies averaged over the three orthogonal polarizations were 0.143, 0.042, and 0.014 at a position near the top of the frame, the bottom of the cavity, and bare planar Ag film, respectively. Note that these

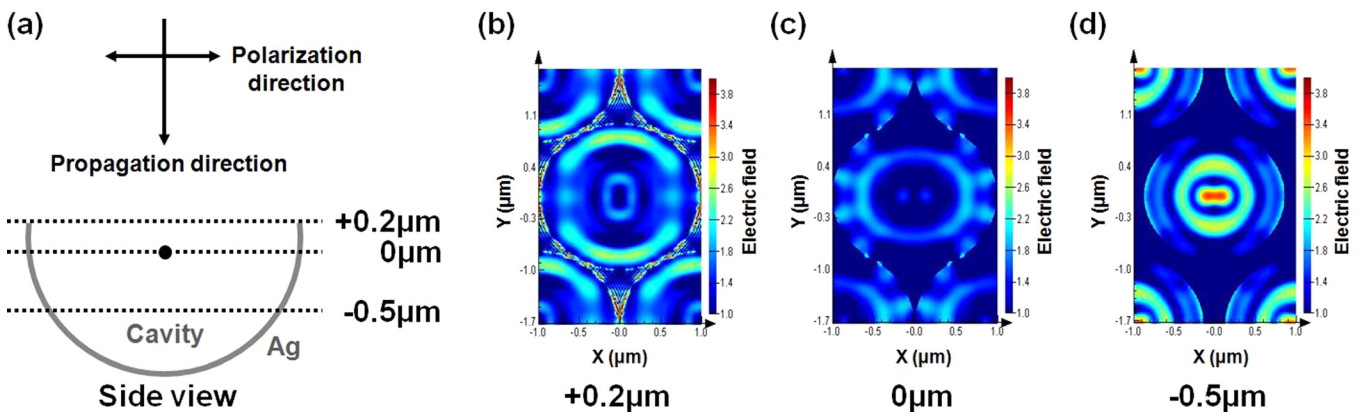

FIG. 4. Electric field distribution around the cavity array of the Ag IO. The theoretical simulation was performed for three arbitrary planes of the Ag IO; (b) top surface located 0.2 μm above, (c) center plane, and (d) inner plane located 0.5 μm below the pivot center, as illustrated in (a).

simulation results correlate qualitatively well with the observed FL intensity images obtained at the top surface and below the pivot center. Quantitatively, the position-dependent field intensity does not correlate linearly with that from the FLIM images. This may be due to coupling between the Ag IO surface and the adjacent dye molecules. Another reason is the surface roughness of the Ag IO film, as observed from the SEM images. In this study, the electric field simulation was calculated without considering the surface roughness and chemical effects. The plane wave and position-dependent dipole calculations suggest that the 3DOM Ag IO structure enhances the fluorescence through position dependent enhancements in the electric field, resulting in the observed enhanced FL phenomenon.

In summary, Ag IO films with micrometer-sized cavities were fabricated by electrochemical deposition using PS opal templates. FLIM imaging showed that the 3DOM Ag IO films provided a stable and uniform platform for FL enhancement. For the rhodamine 123 probe molecule, the Ag frame showed higher FL efficiency than that of the cavity near the top surface of the IO film, whereas the cavity showed better FL efficiency when going to the inner cavity region below the top surface. The non-dispersible and uniform photophysical properties of the film-type metal skeletons are expected to have a variety of applications using film-type porous metal materials in a range of fields, such as ultrasensitive detection and sensing for molecules, proteins, and biological species.

This study was supported by Basic Science Research Program through the National Research Foundation of Korea (NRF) funded by the Ministry of Education (NRF-2015R1D1A1A01058935).

[1]J. R. Lakowicz, Y. Shen, S. D'Auria, J. Malicka, J. Fang, Z. Gryczynski, and I. Gryczynski, Anal. Biochem. **301**, 261–277 (2002).
[2]B. J. Wiley, S. H. Im, Z.-Y. Li, J. McLellan, A. Siekkinen, and Y. Xia, J. Phys. Chem. B **110**, 15666–15675 (2006).
[3]L. Lu, A. Eychmüller, A. Kobayashi, Y. Hirano, K. Yoshida, Y. Kikkawa, K. Tawa, and Y. Ozaki, Langmuir **22**, 2605–2609 (2006).
[4]B. Chen, G. Meng, Q. Huang, Z. Huang, Q. Xu, C. Zhu, Y. Qian, and Y. Ding, ACS Appl. Mater. Interfaces **6**, 15667–15675 (2014).
[5]Y. Zhang, A. Dragan, and C. D. Geddes, J. Phys. Chem. C **113**, 12095–12100 (2009).
[6]W.-S. Chae, H. Yu, S.-K. Ham, M.-J. Lee, J.-S. Jung, and D. B. Robinson, Electron. Mater. Lett. **9**, 783–786 (2013).
[7]T. Singh, Trans. Electr. Electron. Mater. **14**, 172–176 (2013).
[8]J. Zhang, Y. Fu, M. H. Chowdhury, and J. R. Lakowicz, Nano Lett. **7**, 2101–2107 (2007).
[9]E. Fort and S. Grésillon, J. Phys. D: Appl. Phys. **41**, 013001 (2008).
[10]G. Lu, T. Zhang, W. Li, L. Hou, J. Liu, and Q. Gong, J. Phys. Chem. C **115**, 15822–15828 (2011).
[11]H.-O. Lee, E.-M. Kim, H. Yu, J.-S. Jung, and W.-S. Chae, Nanotechnology **20**, 325604 (2009).
[12]S. Zou and G. C. Schatz, Nanotechnology **17**, 2813–2820 (2006).
[13]J. R. Lakowicz, Anal. Biochem. **298**, 1–24 (2001).
[14]J. S. Biteen, D. Pacifici, N. S. Lewis, and H. A. Atwater, Nano Lett. **5**, 1768–1773 (2005).
[15]E. Dulkeith, A. C. Morteani, T. Niedereichholz, T. A. Klar, J. Feldmann, S. A. Levi, F. C. J. M. van Veggel, D. N. Reinhoudt, M. Möller, and D. I. Gittins, Phys. Rev. Lett. **89**, 203002 (2002).
[16]E. Dulkeith, M. Ringler, T. A. Klar, J. Feldmann, A. Munoz Javier, and W. J. Parak, Nano Lett. **5**, 585–589 (2005).
[17]S. K. Ghosh, A. Pal, S. Kundu, S. Nath, and T. Pal, Chem. Phys. Lett. **395**, 366–372 (2004).
[18]P. K. Jain, K. S. Lee, I. H. El-Sayed, and M. A. El-Sayed, J. Phys. Chem. B **110**, 7238–7248 (2006).
[19]K.-S. Lee and M. A. El-Sayed, J. Phys. Chem. B **109**, 20331–20338 (2005).
[20]D. D. Evanof, Jr. and G. Chumanov, J. Phys. Chem. B **108**, 13957–13962 (2004).
[21]W. Ni, X. Kou, Z. Yang, and J. Wang, ACS Nano **2**, 677–686 (2008).
[22]K. Aslan, Z. Leonenko, J. R. Lakowicz, and C. D. Geddes, J. Fluoresc. **15**, 643–654 (2005).
[23]K. Aslan and C. D. Geddes, *Metal-Enhanced Fluorescence* (Wiley, NJ, 2010).
[24]P. Jiang, J. Cizeron, J. F. Bertone, and V. L. Colvin, J. Am. Chem. Soc. **121**, 7957–7958 (1999).
[25]J. Wang, S. Ahl, Q. Li, M. Kreiter, T. Neumann, K. Burkert, W. Knoll, and U. Jonas, J. Mater. Chem. **18**, 981–988 (2008).
[26]P. N. Bartlett, J. J. Baumberg, P. R. Birkin, M. A. Ghanem, and M. C. Netti, Chem. Mater. **14**, 2199–2208 (2002).
[27]J. J. Baumberg, T. A. Kelf, Y. Sugawara, S. Cintra, M. E. Abdelsalam, P. N. Bartlett, and A. E. Russell, Nano Lett. **5**, 2262–2267 (2005).
[28]X. Yu, Y.-J. Lee, R. Furstenberg, J. O. White, and P. V. Braun, Adv. Mater. **19**, 1689–1692 (2007).
[29]Z. A. Sechrist, B. T. Schwartz, J. H. Lee, J. A. McCormick, R. Piestun, W. Park, and S. M. George, Chem. Mater. **18**, 3562–3570 (2006).
[30]F. García-Santamaría, M. Xu, V. Lousse, S. Fan, P. V. Braun, and J. A. Lewis, Adv. Mater. **19**, 1567–1570 (2007).
[31]W.-S. Chae, D. V. Gough, S.-K. Ham, D. B. Robinson, and P. V. Braun, ACS Appl. Mater. Interfaces **4**, 3973–3979 (2012).
[32]See supplementary material at http://dx.doi.org/10.1063/1.4942397 for additional information on the experimental details, instrumentations, and FLIM image data.
[33]M. Y. Berezin and S. Achilefu, Chem. Rev. **110**, 2641–2684 (2010).
[34]W.-S. Chae, E. Choi, Y. K. Jung, J.-S. Jung, and J.-K. Lee, Appl. Phys. Lett. **104**, 153101 (2014).
[35]W. D. Kim, W.-S. Chae, W. K. Bae, and D. C. Lee, Chem. Mater. **27**, 2797–2802 (2015).
[36]J. R. Lakowicz, *Principles of Fluorescence Spectroscopy* (Springer, New York, 2006).
[37]K. Ray and J. R. Lakowicz, J. Phys. Chem. C **117**, 15790–15797 (2013).